Measurement-based quantum lattice gas model of fluid dynamics in 2+1 dimensions

Michael M. Micci and Jeffrey Yepez

Phys. Rev. E **92**, 033302 — Published 1 September 2015

DOI: 10.1103/PhysRevE.92.033302

Measurement-based quantum lattice gas model of fluid dynamics in 2+1 dimensions

Michael M. Micci[1] and Jeffrey Yepez[2,3]
[1]*Department of Aerospace Engineering, The Pennsylvania State University, University Park, Pennsylvania 16802*
[2]*Air Force Research Laboratory/Directed Energy, Kihei, Hawai'i 96753*
[3]*Department of Physics and Astronomy, University of Hawai'i at Manoa, Honolulu, Hawai'i 96822*
(Dated: August 14, 2013)

Presented are quantum simulation results using a measurement-based quantum lattice gas algorithm for Navier-Stokes fluid dynamics in 2+1 dimensions. Numerical prediction of the kinematic viscosity was measured by the decay rate of an initial sinusoidal flow profile. Due to local quantum entanglement in the quantum lattice gas, the minimum kinematic viscosity in the measurement-based quantum lattice gas is lower than achievable in a classical lattice gas. The numerically predicted viscosities precisely match the theoretical predictions obtained with a mean field approximation. Uniform flow profile with double shear layers, on a $16K \times 8K$ lattice, leads to the Kelvin-Helmholtz instability, breaking up the shear layer into pairs of counter-rotating vortices that eventually merge via vortex fusion and dissipate because of the nonzero shear viscosity.

I. INTRODUCTION

An efficient and accurate numerical simulation of the Navier-Stokes equations over large and complex domains, at high Reynolds numbers, and under turbulent flow conditions is of extreme interest to the engineering and scientific community. The availability of an increasing number of processor cores each year has helped to enable a corresponding increase in the simulation domain size and Reynolds number, but algorithms that make the most efficient use of the available parallel computing resources are also needed.

Three main paradigms for addressing the simulation of incompressible viscous fluid dynamics have developed over the years: (1) a macroscopic approach starting with the hydrodynamic equations of motion, (2) a microscopic approach starting with particle dynamics, directly modeling particle motion and particle-particle collisions, and (3) a mesoscopic approach using a kinetic Boltzmann equation of motion.

The first (macroscopic) paradigm starts with the macroscopic governing equations of motion of divergence free flow and the Navier-Stokes equation that, respectively, derive from mass continuity and momentum conservation

$$\nabla \cdot \boldsymbol{v} = 0, \qquad \partial_t \boldsymbol{v} + \boldsymbol{v} \cdot \nabla \boldsymbol{v} = \frac{-\nabla P}{\rho} + \nu \nabla^2 \boldsymbol{v}. \qquad (1)$$

These equations are a closed set with the pressure, P, being determined from a nonlinear Poisson equation found by taking the divergence of the momentum equation. This paradigm employs numerical techniques to deconstruct (1) for computer implementation. Two main methods in this high-level approach have evolved to solve partial differential equations like the classical incompressible flow equations above: spectral methods and stencil-based methods. Spectral methods use assumed basis functions such as a Fourier series for a truncated series expansion of the solution [1]. Test functions are used to ensure that the differential equations are satisfied as closely as possible by the truncated series expansion. In recent work, Schlatter and Orlu [2] have extended the Reynolds number of their simulations up to a value of 4300 by using 3.2×10^9 modes. Stencil-based methods such as the use of finite differences, where the governing equations are discretized and solved for on a grid, sacrifice accuracy in exchange for better parallel performance due to lower communication requirements since only neighboring values need to be communicated. Pirozzoli and Barnardini [3] were recently able to achieve a Reynolds number of approximately 4000 using 34×10^9 grid sites using a finite difference technique. More recent work with a stencil-based method has extended the simulation domain to 4.1×10^{12} grid points through the use of 1.97×10^6 cores [4].

The second (microscopic) paradigm involves the calculation of the motion of particles in such a manner that the Navier-Stokes equations emerge from the particle motion. Molecular dynamics (MD) does this in the most simple and accurate manner by calculating the motions of individual atoms or molecules acted upon by interatomic potentials. Simulations of continuum flows have been shown to match results given by the Navier-Stokes equations [5]. However, the computational resources required to track every individual atom or molecule currently limit MD to low Reynolds numbers due to the small simulation domain sizes [6].

The desire to increase simulation domain size and therefore Reynolds number has led to the development of various lattice-based methods. Lattice-based methods have the ability to incorporate microscopic physics, are able to take advantage of computer processor parallelization, and have reduced memory requirements since particle positions are descretized. The classical lattice gas method solves for the motion of particles having discrete momenta on a discrete lattice subject to both particle collisions and streaming. In 1986 Frisch, Hasslacher, and Pomeau showed that the use of a triangular (Bravais) lattice with six momentum states reproduced isotropic two-dimensional flow as given by the Navier-Stokes equations [7]. In 1987 Frisch *et al.* extended the model to three-

dimensional flows through the use of a four-dimensional face centered hypercube (fchc) lattice, where the three-dimensional flow is obtained by projecting the fchc lattice onto three dimensions [8]. The microscopic method presented here, a quantum mechanical generalization of the classical lattice gas method, is called the quantum lattice gas method.

The third (mesoscopic) paradigm starts with a Boltzmann equation model of collisional processes in gases [9]. In the kinetic Boltzmann equation method the collision operator includes terms in a hierarchy of particle-particle interactions. This hierarchy can be cut off and the collision operator linearized, such as in the Bhatnager-Gross-Krook (BGK) approximation [10], to direct the flow distribution function toward a local equilibrium chosen to be the Maxwellian distribution. When implemented on a discrete spacetime, this kinetic method becomes the lattice Boltzmann method [11]. The lattice Boltzmann method was originally developed as a computational fluid dynamics technique to reduce the statistical noise inherent in the classical lattice gas, and the method was usually implemented in the BGK approximation [12–14]. However, the lattice Boltzmann method in the BGK approximation suffers from numerical instability as the viscosity is reduced in order to increase the simulation Reynolds number.

To alleviate this problem, the entropic lattice Boltzmann method (ELB) has been developed to replace the lattice BGK linear collision approximation — particle-particle interactions are generated using an appropriate Lyapunov functional to model the collisional process [15, 16]. The Lyapunov functional determines both the equilibrium distribution and the path to that distribution and thus can be used to control the stability properties of the model. Vahala *et. al.* [17] used ELB to calculate turbulence characteristics at a Reynolds number of 25,000 by using a 1600^3 grid and found excellent agreement with Large Eddy Simulation lattice Boltzmann (LES-LB) results. A quantum lattice gas model, such as the particular one presented below, can also be implemented as a mesoscopic model and in this case is referred to as a quantum lattice Boltzmann equation model [18].

II. QUANTUM LATTICE GAS METHOD

Quantum computing and the development of quantum algorithms represent a paradigm shift in the way computing is done. Whereas a single bit (the smallest unit of memory storage in a classical digital computer) can only have one of two values, 0 or 1, quantum computing is based on a quantum state of a qubit, which is the superposition of the two discrete quantum states $|0\rangle$ and $|1\rangle$. The qubit state $|q\rangle$ is thus $\alpha|0\rangle + \beta|1\rangle$, where $|\alpha|^2$ and $|\beta|^2$ are the probabilities of the qubit being in either of the two respective states. The values of the complex coefficients α and β are constrained by $|\alpha|^2 + |\beta|^2 = 1$ such that the probability of the qubit being in the $|0\rangle$ state plus the probability of it being in the $|1\rangle$ state is unity. So quantum computing offers a new way to address the problem of modeling fluid dynamics. One generalization of the classical lattice gas method is a measurement-based quantum lattice gas algorithm [18, 19]. An overview description of the quantum lattice gas model of quantum computation is given in Ref. [20], and numerical results obtained by a supercomputer implementation of incompressible viscous fluid flow in 2+1 dimensions are reported below.

Computation can be reversible when implemented as a microscopic quantum algorithm. For a reversible algorithm, a unitary evolution operator, $e^{-i\hat{H}\tau/\hbar}$, can be specified that acts at time t on the total system wave function, $|\Psi(t)\rangle$, which constitutes the state of all the qubits or the quantum computer's memory. If there are n qubits, the quantum space $|\Psi(t)\rangle$ occupies an exponentially large Hilbert space with 2^n dimensions. A new quantum state at a later time, $|\Psi(t+\tau)\rangle$, is obtained by application of the unitary operator, which can be represented by a unitary matrix of size 2^nx 2^n

$$|\Psi(t+\tau)\rangle = e^{-i\hat{H}\tau/\hbar}|\Psi(t)\rangle, \tag{2}$$

where n is the number of qubits in the system. Thus a solution for the system state at a later time requires a single computational step on a quantum computer, and the computational step is the same regardless of the number of particles in the quantum simulation. It has also been found serendipitously that quantum algorithms for the solution of a variety of mathematical problems, even when implemented on classical computers, can provide a significant computational speedup [20–26].

The Hamiltonian $\hat{H} = \hat{H}_\circ + \hat{H}'$ contains both a free kinetic energy part $\hat{H}_\circ$ and a particle-particle interaction part $\hat{H}'$. These two parts of the hermitian generator are decomposed into two distinct operators and separated by a measurement operation, such that the reversible evolution operator $e^{-i\hat{H}\tau/\hbar}$ is converted to a dissipative evolution operator $e^{-i\tilde{H}_\circ\tau/\hbar}\,\hat{\Gamma}\,e^{-i\tilde{H}'\tau/\hbar}$, where we use the tilde symbol to denote the lattice-gas generators.[1] This represents the measurement step. The collide operator $\hat{\mathcal{C}} \equiv e^{-i\tilde{H}'\tau/\hbar}$ creates entangled cluster states at every point in the system. After that (post-collision), the operator $\hat{\Gamma} \equiv \hat{\mathcal{I}}\hat{\mathcal{P}}$ causes collapse of the entangled cluster state via operator $\hat{\mathcal{P}}$ and then injects this state back into the full Hilbert space by tensor product operator $\hat{\mathcal{I}}$. Finally (post-measurement), the stream operator $\hat{\mathcal{S}} \equiv e^{-i\tilde{H}_\circ\tau/\hbar}$

[1] Since $[\hat{H}_\circ, \hat{H}'] \neq 0$, we know that $e^{-i\hat{H}_\circ\tau/\hbar} \neq e^{i\hat{H}'\tau/\hbar}e^{-i\hat{H}\tau/\hbar}$. However, there exists hermitian generators $\tilde{H}_\circ$ and $\tilde{H}'$ such that $e^{-i\tilde{H}_\circ\tau/\hbar}e^{i\tilde{H}'\tau/\hbar} \approx e^{-i\tilde{H}\tau/\hbar}$ to very high-order accuracy when entanglement in the quantum state is localized to the Hilbert subspace at a point, and this localization is represented by $\hat{\Gamma}$ [27]. So the hermitian generators in (3) are akin (but are not equal) to their counterparts in (2), i.e. $\tilde{H}_\circ \neq \hat{H}_\circ$ and $\tilde{H}' \neq \hat{H}'$.

models the free particle motion confined to the lattice. The effective hydrodynamics behavior of the quantum lattice gas algorithm for modeling a Navier-Stokes fluid is tested here via quantum simulations carried out using the measurement-based quantum algorithm

$$|\Psi(t+\tau)\rangle = e^{-i\tilde{H}_\circ \tau/\hbar}\hat{\Gamma}e^{-i\tilde{H}'\tau/\hbar}|\Psi(t)\rangle. \quad (3)$$

The measurement-based quantum lattice gas (3) originally proposed as a practical algorithm for computational fluid dynamics [28] is tested here in various 2+1 dimensional simulations. We find that (3) is a valid representation of (1).

The measurement-based quantum lattice gas is a generalization of a classical lattice gas. A classical lattice gas algorithm for fluid dynamics in 2+1 dimensions was developed by Frisch, Hasslacher, and Pomeau, and it is known a the FHP model [7]. The occupancy probability of the momentum state along the ath lattice direction at a point in the lattice is given by Boolean number variable $n_a \in [0,1]$. In the quantum lattice gas algorithm developed by Yepez [19, 20, 28], the occupancy probability amplitude of the momentum state along the ath lattice direction at a point is given by the quantum state of a qubit $|q_a\rangle$, which is a superposition of logical "zero" state $|0\rangle = \begin{pmatrix}1\\0\end{pmatrix}$ and the logical "one" state $|1\rangle = \begin{pmatrix}0\\1\end{pmatrix}$, at that point. The classical Boolean number variable is recovered by taking the expectation value of the singleton number operator, $n_a = \langle q_a|\hat{n}|q_a\rangle = 0$ when $|q_a\rangle = |0\rangle$ and $n_a = \langle q_a|\hat{n}|q_a\rangle = 0$ when $|q_a\rangle = |1\rangle$, where $\hat{n} = \begin{pmatrix}0&0\\0&1\end{pmatrix}$. However, as mentioned in the introduction, in general $|q_a(x)\rangle = \alpha(x)|0\rangle + \beta(x)|1\rangle$ is a superposition state, where the c-numbers are constrained by bit conservation $|\alpha(x)|^2+|\beta(x)|^2$. Then, the real-valued occupancy probability of the ath momentum state at a point x is given by $f_a(x) = \langle q_a(x)|\hat{n}|q_a(x)\rangle = |\beta(x)|^2$, which is a kinetic variable represented at the mesoscopic scale. Six qubits for the six momentum states are assigned to each point in the lattice, where each qubit at x is determined by the occupancy probability by

$$|q_a(x)\rangle = \sqrt{f_a}(x)|1\rangle + \sqrt{1-f_a(x)}|0\rangle. \quad (4)$$

Because there are $Q = 6$ qubits per point, there are $2^6 = 64$ dimensions in the local Hilbert space per point. Each numbered state is represented by the incoming on-site ket given by the tensor product of the six qubits

$$|\psi(x)\rangle = \bigotimes_{a=1}^{Q} |q_a(x)\rangle. \quad (5)$$

The number states may be labelled by a 6-bit integer $N \in [0,63]$, i.e. $|N\rangle = |n_1 n_2 \ldots n_6\rangle$, where n_a are Boolean number variables. The local ket at point x is in general the quantum state

$$|\psi(x)\rangle = \sum_{N=0}^{2^Q-1} \psi_N(x)|N\rangle = \begin{pmatrix}\psi_0(x)\\ \psi_1(x)\\ \vdots \\ \psi_{2^Q-1}(x)\end{pmatrix}, \quad (6)$$

where $\psi_N(x)$ is the c-number probability amplitude for the numbered state $|N\rangle$, and the full quantum state is formed as a tensor product over all spatial points of the lattice, $|\Psi(t)\rangle = \bigotimes_{x\in\text{lattice}} |\psi(x,t))\rangle$. Defining an on-site collision operator, $\hat{U}$, the post collision ket $|\psi'(x)\rangle$ is given by

$$|\psi'(x)\rangle = \hat{U}|\psi(x)\rangle, \quad (7)$$

and the outgoing (post-collision) occupancy probability distribution is given by

$$f'_a(x) = \langle\psi(x)|\hat{U}^\dagger\hat{n}_a\hat{U}|\psi(x)\rangle = \langle\psi'(x)|\hat{n}_a|\psi'(x)\rangle, \quad (8)$$

where the multiple qubit number operator for the ath qubit has the singleton number operator at the ath position, i.e. $\hat{n}_a \equiv \mathbf{1}^{\otimes(a-1)} \otimes \hat{n}$. Each probability is then streamed to its neighboring lattice site and the process is repeated. In the quantum lattice gas algorithm, the unitary evolution operator in (2) is decomposed into the product of unitary stream and collision operators, $e^{-i\hat{H}\tau/\hbar} = \hat{S}\hat{C}$, where the $\hat{C} = \bigotimes_x \hat{U}$.

In measurement-based quantum lattice gas form, the decomposition (3) can be written as a strongly-correlated many-body quantum evolution equation

$$|\Psi(x_1,...,x_n;t+\tau)\rangle = \hat{S}\,\hat{\Gamma}\,\hat{C}|\Psi(x_1,...,x_n;t)\rangle, \quad (9)$$

where $\hat{S}$ is a unitary streaming operator and $\hat{C} = \bigotimes_x \hat{U}$ is a tensor product of the local complex unitary collision operator, analogous to the collision operator in the classical lattice gas. $\hat{U}$ causes entanglement of the outgoing collision configurations at each point of the lattice. Characteristic of a measurement-based quantum algorithm, the local evolution (9) contains a projection operator, denoted here by $\hat{\Gamma}$, and this operator collapses each entangled cluster state that exists at every point of the system. $\hat{\Gamma}$ can be implemented on a measurement-based quantum computer by Von Neuman projective measurement of the qubits in the system. Because of $\hat{\Gamma}$, (9) represents dissipative particle dynamics, which becomes equivalent to (1) in the continuum limit. The stream operator, $\hat{S}$, is an orthogonal permutation matrix with components being either 0 or 1. It causes particles to move from one site to the next and causes global shift the qubit occupations. Yepez derived unitary collision operators that reproduced the lattice Boltzmann equation, and thus the viscous Navier-Stokes equations, at the mesoscale [19, 20, 28]. He showed that detailed balance is obeyed and that the method is noiseless and unconditionally stable.

Yepez's analytical result from Refs. [19, 20] is that the effective equation of motion for flow field $\boldsymbol{v}$ and fluid

density ρ for a quantum lattice gas in D spatial dimensions reduces to the following flow equation in the long-wavelength, low-frequency, and subsonic limits:

$$\partial_t(\rho v_i) + \partial_j \Pi_{ij} + \cdots = 0, \tag{10}$$

where the momentum flux density is

$$\Pi_{ij} = P_{ij} + g\rho v_i v_j - \frac{\rho \ell^2}{(D+2)\tau}\left(\frac{1}{\kappa_\eta} - \frac{1}{2}\right)\partial_j v_i, \tag{11}$$

and where the lattice cell size is $\ell = c\tau$ for the unit speed c. With sound speed $c_s \equiv \ell/(\tau\sqrt{D})$, the pressure tensor is a bilinear functional of the fluid flow

$$P_{ij} = \rho c_s^2 \left(1 - g\frac{v^2}{c^2}\right)\delta_{ij}, \tag{12}$$

with the density-dependent factor

$$g(d) = \frac{D}{D+2}\frac{1-2d}{1-d}, \tag{13}$$

where the reduced density is $d = \rho/B$ and B is the lattice coordination number (i.e. $B = 6$ for the triangular lattice). Finally, inserting (11) into (10), the momentum equation for viscous flow is

$$\begin{aligned} &\partial_t(\rho v_i) + \partial_j(g\rho v_i v_j) = \\ &-\partial_i P + \eta\partial^2 v_i + \left(\zeta + \frac{\eta}{D}\right)\partial_i\partial_j v_j + \cdots, \end{aligned} \tag{14}$$

with shear viscosity

$$\eta = \frac{\rho\ell^2}{\tau}\frac{1}{D+2}\left(\frac{1}{\kappa_\eta} - \frac{1}{2}\right), \tag{15}$$

and bulk viscosity

$$\zeta = \frac{\rho\ell^2}{\tau}\frac{2D-1}{D(D+2)}\left(\frac{1}{\kappa_\eta} - \frac{1}{2}\right), \tag{16}$$

where κ_η is the viscosity eigenvalue of the Jacobian matrix with components $J_{ab} = \partial\Omega_a/\partial f_b|_{f^{\text{equil.}}=d}$ and where the form of the collision operator Ω_a in the quantum lattice gas model is explained below. With small Knudsen, Strouhal, and Mach numbers, the momentum equation (14) approximates the Navier-Stokes equation in (1) with $g(d)$ appearing in the convective and pressure terms in (14).

If $g(d)$ is positive definite but less than unity for some particular value of d used in a flow simulation, then one simply rescales velocity field $\boldsymbol{v} \to g\boldsymbol{v}$ to ensure that the momentum flow equation is Galilean invariant. Furthermore, when modeling fluid flow with characteristic flow speed U, the density-dependent factor $g > 0$ may be chosen to be proportional to or less than the Mach number ($g(d) \lessapprox U/c = M$) by choosing $d \lessapprox 1/2$ so that the pressure $P = \rho c_s^2 + \mathcal{O}(\mathrm{M}^3)$ becomes effectively isotropic and velocity independent, to within the level of approximation employed in the model. So like the lattice Boltzmann equation method for compressible flow constrained to low Mach number, the pressure term in the quantum lattice gas also becomes proportional to the density.

We provide the following numerical demonstrations below. We test the quantum lattice gas in its classical lattice gas representation and then we test the quantum lattice gas as a quantum algorithm that exploits local entanglement. As part of both these tests, we carry out numerical measurements reported below that include incompressible fluid simulations of viscous decay and the Kelvin-Helmholtz shear instability.

A. Classical lattice gas as a special case

Two-body, three-body, four-body, and two-body with a spectator particle collisions were incorporated into the algorithm in order to lower the viscosity and increase the Reynolds number of the simulations as much as possible. An example of a two-body collision with even and odd chirality is shown in Fig. 1(a). A three-body collision, shown in Fig. 1(b), has only one possible outcome. A four-body collision has two possible outcomes depending on the chirality as is shown in Fig. 1(c). Finally, a two-body collision with a spectator particle, an example of which is shown in Fig. 3(d), has, as in the case of three-body collisions, only one possible outcome.

By the correspondence principle, quantum mechanics leads to classical mechanics by the Ehrenfest theorem. The particle dynamics represented by a quantum lattice gas is a superset of the particle dynamics represented by a classical lattice gas. So it possible to use a quantum lattice gas algorithm to represent a classical lattice gas, albeit without the shot noise—and this correspondence is a first test of our quantum method reported herein.

The classical (albeit unitary) collision matrix for three-body and two-body with a spectator particle collisions is an orthogonal O(2) matrix of the form

$$\hat{U}^{\text{classical}}_{\text{3-body}} = \begin{pmatrix} 0 & 1 \\ 1 & 0 \end{pmatrix} \tag{17}$$

with no free parameters. Thus following (7), the collision shown in Fig. 1(b) can be written as

$$\begin{pmatrix} \psi'_{21} \\ \psi'_{42} \end{pmatrix} = \hat{U}^{\text{classical}}_{\text{3-body}} \begin{pmatrix} \psi_{21} \\ \psi_{42} \end{pmatrix} \tag{18}$$

where the two states are switched at each collision. The collision matrix for two and four-body collisions is an orthogonal O(3) operator of the form

$$\hat{U}^{\text{classical}}_{\text{2-body}} = \begin{pmatrix} 0 & 1 & 0 \\ 0 & 0 & 1 \\ 1 & 0 & 0 \end{pmatrix}, \tag{19}$$

and its transpose, where (19) and its transpose are applied at alternating time steps. Again, following (7), the

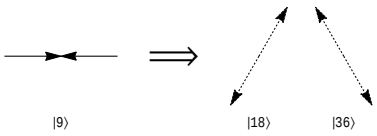

(a) a 2-body state $|9\rangle$ transitions to state $|18\rangle$ or $|36\rangle$

(b) a 3-body state transition, and the reverse transition occurs too

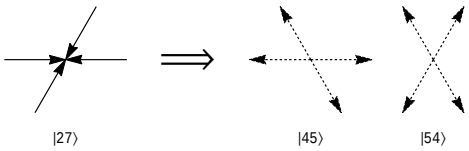

(c) a 4-body state $|27\rangle$ transitions to state $|45\rangle$ or $|54\rangle$

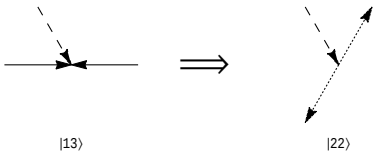

(d) 2-body state transition with a spectator particle (dashed line)

FIG. 1: Examples of particle-particle collisions in a classical lattice gas confined to a two-dimensional hexagonal lattice. The collisions show particle momenta with incoming states (solid) transitioning to outgoing states (dotted). All single particle momentum vectors are unit magnitude and are along the hexagonal lattice directions. The value within the ket is the number of the shown state out of the possible $2^6 = 64$ states in the Hilbert space as given by (5). The other particle-particle collisions are obtained by cyclic permutations of these.

collision shown in Fig. 1(a) can be written as

$$\begin{pmatrix} \psi'_9 \\ \psi'_{18} \\ \psi'_{36} \end{pmatrix} = \hat{U}^{\text{classical}}_{\text{2-body}} \begin{pmatrix} \psi_9 \\ \psi_{18} \\ \psi_{36} \end{pmatrix}, \tag{20}$$

where the three states are permuted at each collision.

A two-dimensional Bravais lattice with periodic boundary conditions was constructed, with a collision and stream operation performed sequentially at each lattice site for each time step to update the probabilities of the six momentum directions. Kinematic viscosities of the simulated fluids were computed by simulating the exponential decay of an initial sinusoidal velocity oscillation for the cases of a) two and three-body collisions, b) two, three, and four-body collisions, and c) two, three, four, and two-body with a spectator particle collisions. Analytical expressions for the kinematic viscosity were obtained using the mean field approximation by calculating the degenerate eigenvalues of the Jacobian of the collision operator evaluated at equilibrium [29], where the collision operator is given by

$$\Omega_a = f'_a - f_a = \langle\psi|\hat{U}^\dagger \hat{n}_a \hat{U} - \hat{n}_a|\psi\rangle. \tag{21}$$

For two and three-body collisions, the kinematic viscosity as a function of the reduced density, d, is given by

$$\nu = \frac{1}{12d(1-d)^3} - \frac{1}{8}. \tag{22}$$

where $0 \le d \le 1$ is the probability of occupancy of a point when the system is under the condition of global thermodynamic equilibrium. For two, three, and four-body collisions the kinematic viscosity (that is manifestly particle-hole symmetric) is given by

$$\nu = \frac{1}{12d(1-d)^3 + 12(1-d)d^3} - \frac{1}{8}, \tag{23}$$

and for two, three, four, and two-body with a spectator particle collisions the kinematic viscosity is given by

$$\nu = \frac{1}{3d(1-d)^3 + 12d^2(1-d)^2 + 3(1-d)d^3} - \frac{1}{8}. \tag{24}$$

The computed viscosities as a function of reduced density were found to match the values given by the classical mean field approximation over the entire range of densities, shown in Fig. 2. So with the appropriate special

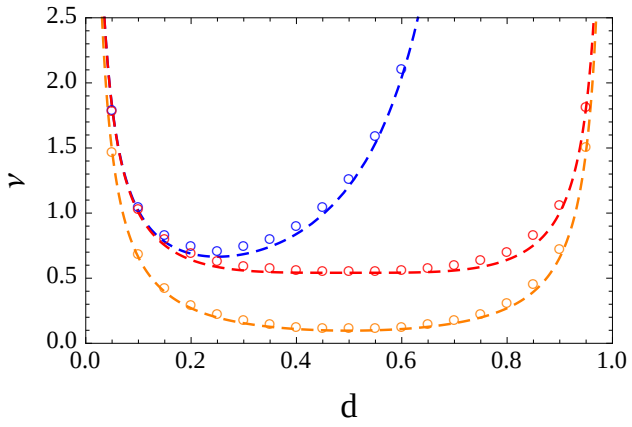

FIG. 2: (Color online) Kinematic viscosity as a function of reduced density, d. Dashed lines show the mean field approximation results. Blue (dark) is two and three-body collisions, red (middle) is two, three, and four-body collisions, and orange (light) is two, three, four, and two-body with a spectator particle collisions.

case unitary collision operator, the quantum lattice gas behaves as a classical lattice gas. However, since probability amplitudes of a qubit are used to encode particle occupation, the shot-noise that is otherwise characteristic (and a drawback) of the classical lattice gas is altogether eliminated in the quantum lattice gas in this special limit.

The collision operators (17) and (19) do not induce any quantum entanglement, so no projection operation is required prior to particle streaming. Thus, the operative quantum algorithm in this special limit has the classic form $|\Psi(t+\tau)\rangle = e^{-i\hat{H}_\circ \tau/\hbar} e^{-i\hat{H}'\tau/\hbar}|\Psi(t)\rangle = \hat{S}\hat{C}|\Psi(t)\rangle$ of a lattice gas model. This evolution is just the usual stream-collide decomposition of (2).

B. Measurement-based quantum lattice gas

The classical lattice gas algorithm was converted into a quantum lattice gas algorithm following the work of Yepez. The collision matrix for three-body and two-body with a spectator particle collisions is an SU(2) matrix of the form

$$\hat{U}^{\text{quantum}}_{\text{3-body}} = \begin{pmatrix} e^{i\zeta}\cos\eta & e^{i\xi}\sin\eta \\ -e^{-i\xi}\sin\eta & e^{-i\zeta}\cos\eta \end{pmatrix} \tag{25}$$

with three free parameters: ζ, ξ, and η. Following (7), the collision shown in Fig. 3(b) can be written as

$$\begin{pmatrix} \psi'_{21} \\ \psi'_{42} \end{pmatrix} = \hat{U}^{\text{quantum}}_{\text{3-body}} \begin{pmatrix} \psi_{21} \\ \psi_{42} \end{pmatrix} \tag{26}$$

where the two states ψ_{21} and ψ_{42} are now entangled at each collision.

The SU(3) collision matrix for two and four-body collisions is obtained by combining the appropriate three Gell-Mann matrices, (see appendix for the matrix representation of λ_i for $i = 1, 2, \ldots, 8$), via

$$\hat{U}^{\text{quantum}}_{\text{2-body}} = e^{i\theta(-\lambda_2+\lambda_5-\lambda_7)} \tag{27}$$

with θ as the single free parameter. The degenerate eigenvalues of the Jacobian of the collision operator evaluated at equilibrium, i.e., the viscosity, are real only for a value of $\theta = 3\pi/\sqrt{3}$, giving the $\sqrt{\text{SWAP}}$ unitary operator of the form

$$\hat{U}^{\text{quantum}}_{\text{2-body}} = \begin{pmatrix} -\frac{1}{3} & \frac{2}{3} & \frac{2}{3} \\ \frac{2}{3} & -\frac{1}{3} & \frac{2}{3} \\ \frac{2}{3} & \frac{2}{3} & -\frac{1}{3} \end{pmatrix}. \tag{28}$$

The three parameters (ζ, η, ξ) are now available to vary the viscosity. The outgoing entangled cluster states for the four types of collisions are shown in Fig. 3. Again, following (7), the collision shown in Fig. 3(a) can be written as

$$\begin{pmatrix} \psi'_{9} \\ \psi'_{18} \\ \psi'_{36} \end{pmatrix} = \hat{U}^{\text{quantum}}_{\text{2-body}} \begin{pmatrix} \psi_{9} \\ \psi_{18} \\ \psi_{36} \end{pmatrix}, \tag{29}$$

where the three states are entangled at each collision.

Kinematic viscosities were again computed by simulating the exponential decay of an initial sinusoidal velocity oscillation and calculated analytically via the mean field approximation as for (22)-(24) for the same three cases.

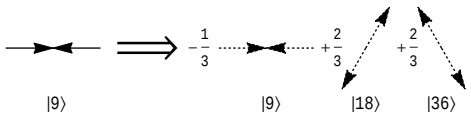

(a) a 2-body state $|9\rangle$ transitions to the entangled cluster state $-\frac{1}{3}|9\rangle + \frac{2}{3}|18\rangle + \frac{2}{3}|36\rangle$

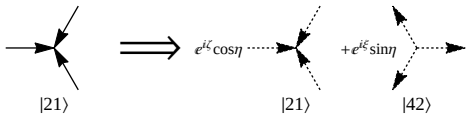

(b) a 3-body state $|21\rangle$ transitions to the entangled cluster state $e^{i\zeta}\cos\eta|21\rangle + e^{i\xi}\sin\eta|42\rangle$

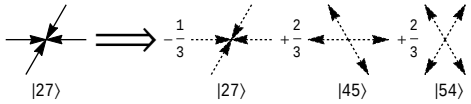

(c) a 4-body state $|27\rangle$ transitions to the entangled cluster state $-\frac{1}{3}|27\rangle + \frac{2}{3}|45\rangle + \frac{2}{3}|54\rangle$

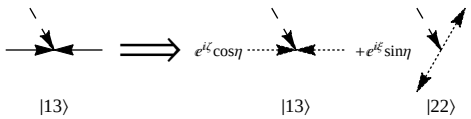

(d) state $|13\rangle$, 2-body with a spectator particle (dashed line), transitions to entangled cluster state $e^{i\zeta}\cos\eta|13\rangle + e^{i\xi}\sin\eta|22\rangle$

FIG. 3: Examples of particle-particle collisions in a quantum gas confined to a two-dimensional hexagonal lattice. The collisions show particle momenta with incoming states (solid) transitioning to outgoing states (dotted). All single particle momentum vectors are unit magnitude and are along the hexagonal lattice directions.

The kinematic viscosity given by the mean field approximation for two and three-body collisions is

$$\nu = \frac{1}{16d(1-d)^3} - \frac{1}{8}. \tag{30}$$

For two, three, and four-body collisions the kinematic viscosity (that is manifestly particle-hole symmetric) is given by

$$\nu = \frac{1}{16d(1-d)^3 + 16(1-d)d^3} - \frac{1}{8}, \tag{31}$$

and for two, three, four, and two-body with a spectator particle collisions the kinematic viscosity is given by

$$\nu = \frac{1}{4d(1-d)^3 + 12d^2(1-d)^2 + 4(1-d)d^3} - \frac{1}{8}. \tag{32}$$

Because of the quantum superposition of states none of the kinematic viscosities are dependent on the three SU(2) parameters in (25), which in this case were $\eta = \frac{\pi}{2}$ and $\zeta = \xi = 0$. It is shown in Fig. 4 that for all three cases the minimum viscosity as a function of reduced density computed in the quantum lattice gas algorithm was lower

than that computed in the classical lattice gas algorithm due to the entangled output states in the quantum lattice gas following each collide step. The viscosities computed with the quantum lattice gas algorithm also agreed with those given by the mean field approximation.

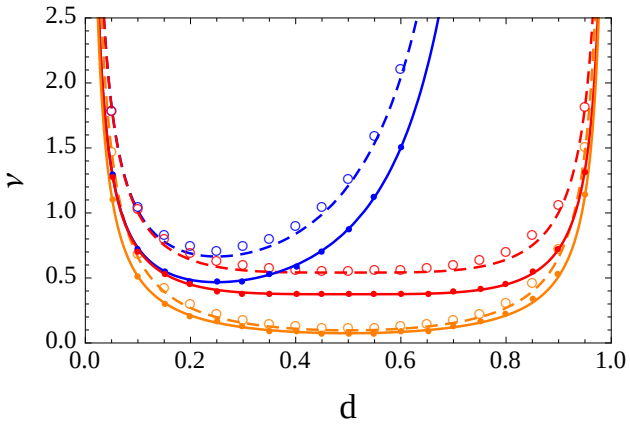

FIG. 4: (Color online) Kinematic viscosity as a function of reduced density, d. Lines show the mean field approximation results, dashed for classical lattice gas and solid for quantum lattice gas. Blue (top pair) is two and three-body collisions, red (middle pair) is two, three, and four-body collisions, and orange (bottom pair) is two, three, four, and two-body with a spectator particle collisions.

The quantum lattice gas algorithm was then modified to simulate a shear flow and the resulting development of Kelvin-Helmholtz instabilities. The computational domain consisted of 16384×8192 Bravais lattice sites for a total of 1.34×10^8 points with the initial flows in the long dimension and periodic boundary conditions on all sides. A strip of 1024 lattice sites in the middle of the domain was initialized with a velocity of 0.28 while the domains on each side of this strip were initialized with a velocity of 0.04 in the opposite direction for an initial total system momentum of zero. The value of the reduced density, d, was 0.17. Random noise with an amplitude of 5% was added to the initial velocities. As for the classical lattice gas, a collision and stream operation were performed sequentially at each lattice site for each time step to update the probabilities of the six momentum directions.

The algorithm was parallelized using MPI and was run using from 256 to 4096 processor cores, achieving a maximum site update rate on 4096 cores of 2.43×10^9 lattice sites per second and a wall clock run time of approximately 90 minutes to complete 100,000 time steps. The wall clock run time scaled approximately with the inverse of the number of cores up to 2048 cores. At 4096 cores the communication required for the outputting of the plot and continuation files began to consume a significant amount of the total run time. Memory requirements are low as, in theory, only six values are stored for each lattice point and each processor only needs the values for its lattice points and those on two of its boundaries. Although the algorithm was optimized for speed, the processors were shown to be able to handle at least 524,288 lattice nodes each, enabling a future expansion of the algorithm to three dimensions.

Fig. 5(b) shows a contour plot of the initial vorticity, showing the shear layer with opposite vorticity on each side of the center upward flow. By 100,000 time steps, shown in Fig. 5(c), it can be seen that an instability is starting to develop in the shear layer. This instability then rapidly grows, and as shown in Fig. 5(d), by 150,000 time steps separate vortices are beginning to break off. The breakup of the shear layer completes around 200,000 time steps, shown in Fig. 5(e). Figs. 5(f) and 5(g) show the vortices at 400,000 and 700,000 time steps respectively, where merging and dissipation of the vortices have occurred. From this point on the vortices dissipate, with the last one dropping below the contour color level at approximately 1,119,000 time steps.

III. CONCLUSION

A quantum lattice gas model of Navier-Stokes fluid dynamics (i.e. incompressible flow limit) in 2+1 dimensions was tested as a candidate computational fluid dynamics algorithm. The quantum algorithm was parallelized using MPI to increase the domain size and therefore the Reynolds number, reduce the run time, and take advantage of the computational resources available at the MHPCC. Four types of collisions were incorporated: two particle, three particle, four particle, and two particle with a spectator particle. The quantum lattice gas model can incorporate unitary collision operators that induce classical particle-particle collisions or quantum mechanical particle-particle collisions, the latter producing locally entangled states. Numerical simulations were conducted for both classical and quantum collisions, and in the former case the fluid dynamics in a classical lattice gas is reproduced. Even though the computational effort for the quantum lattice algorithm is similar to that for a classical lattice gas, the case of quantum collisions is important because of its potential to reduce the shear viscosity compared to the classical lattice gas when incorporating the same collision types in the modeled fluid and thus achieve a high level of convective nonlinearity in the flow. The quantum lattice algorithm is reversible and noiseless, and provides an algorithm that can be implemented on measurement-based quantum computers as they become available.

Calculation of the fluid viscosity was conducted by simulating the decay of an initial sinusoidal flow profile. Due to the local quantum entanglement of states in a quantum lattice gas, the minimum fluid viscosities for the quantum lattice gas algorithm were lower than those obtained by a classical lattice gas algorithm, and the viscosities matched analytical values given by the mean field approximation. A shear layer producing a Kelvin-Helmholtz instability was then simulated on a $16K \times 8K$ lattice with the quantum lattice gas algorithm. Instability of

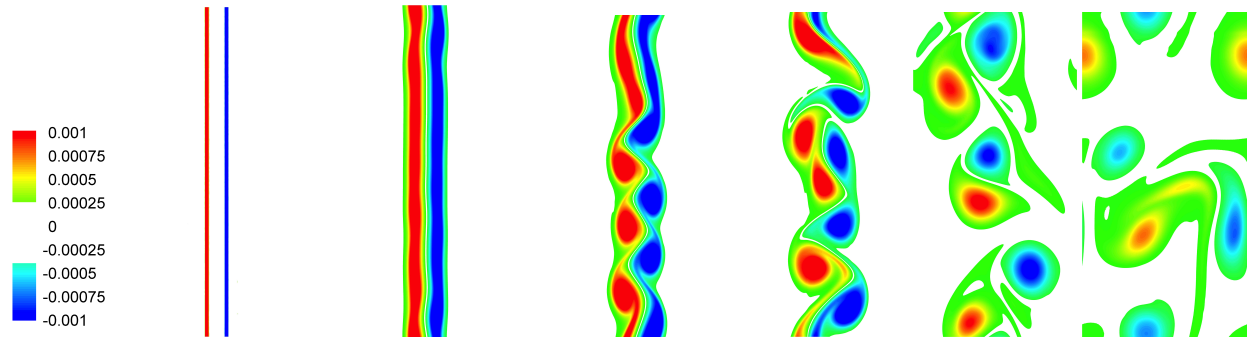

(a) $|\nabla \times \boldsymbol{v}|$ (b) $t = 0$ (c) $t = 100K$ (d) $t = 150K$ (e) $t = 200K$ (f) $t = 400K$ (g) $t = 700K$

FIG. 5: (Color online) Contour plot of vorticity at initialization. Center flow is upward at a velocity of 0.28, and outer flow is downward at a velocity of 0.04 with a background density of $d = 0.17$. Start of the KH instability occurs around 100,000 time steps. By 150,000 time steps, the KH instability causes the breakup of the shear layer into separate vortex pairs. By 400,000 time steps, dissipation begins to dominate the flow. By 700,000 time steps merging of the vortices has started.

the shear layer resulting in the breakup of the shear layer into separate vortices that then merge and dissipate was observed. The numerical behavior of the quantum lattice gas model precisely matched the theoretically predicted behavior in test cases.

IV. ACKNOWLEDGEMENTS

This research was supported by grants from the Air Force Office of Scientific Research, the National Research Council, and the DoD High Performance Computing Modernization Program. Supercomputer resources were provided for the Air Force Research Laboratory's Maui High Performance Computing Center.

[1] C. Canuto, M. Hussaini, A. Quarteroni, and T. Zang, *Spectral Methods in Fluid Dynamics* (Springer-Verlag, New York, 1988).

[2] P. Schlatter and R. Örlü, Journal of Fluid Mechanics **659**, 116 (2010), ISSN 1469-7645, URL http://journals.cambridge.org/article_S0022112010003113.

[3] S. Pirozzoli and M. Bernardini, Physics of Fluids (1994-present) **25**, 021704 (2013), URL http://scitation.aip.org/content/aip/journal/pof2/25/2/10.1063/1.4792164.

[4] I. Bermejo-Moreno, J. Bodart, J. Larsson, B. Barney, J. Nichols, and S. Jones, in *Proceedings of the International Conference on High Performance Computing, Networking, Storage and Analysis* (ACM, New York, NY, USA, 2013), SC '13, pp. 62:1–62:10, ISBN 978-1-4503-2378-9, URL http://doi.acm.org/10.1145/2503210.2503265.

[5] J. Koplik and J. R. Banavar, Annual Review of Fluid Mechanics **27**, 257 (1995), http://dx.doi.org/10.1146/annurev.fl.27.010195.001353, URL http://dx.doi.org/10.1146/annurev.fl.27.010195.001353.

[6] K. F. Ludwig and M. Micci, Atomization and Sprays **21**, 275 (2011), ISSN 1044-5110.

[7] U. Frisch, B. Hasslacher, and Y. Pomeau, Phys. Rev. Lett. **56**, 1505 (1986), URL http://link.aps.org/doi/10.1103/PhysRevLett.56.1505.

[8] U. Frisch, D. d'Humieres, B. Hasslacher, P. Lallemand, Y. Pomeau, and J.-P. Rivet, Complex Systems **1**, 649 (1987).

[9] P. L. Bhatnagar, E. P. Gross, and M. Krook, Phys. Rev. **94**, 511 (1954).

[10] E. P. Gross and E. A. Jackson, Physics of Fluids **2**, 432 (1959), URL http://link.aip.org/link/?PFL/2/432/1.

[11] S. Succi, *The Lattice Boltzmann Equation for Fluid Dynamics and Beyond* (Clarendon Press, Oxford, 2001).

[12] S. S. R. Benzia and M. Vergassola, Physics Reports **222**, 145 (1992).

[13] Y. Qian, D. d'Humiéres, and P. Lallemand, Europhysics Letters **17**, 479 (1992).

[14] D. O. Martinez, W. H. Matthaeus, S. Chen, and D. Montgomery, Physics of Fluids **6**, 1285 (1994).

[15] I. V. Karlin, A. Ferrante, and H. C. Ottinger, Europhysics Letters **47**, 182 (1999).

[16] B. M. Boghosian, J. Yepez, P. V. Coveney, and A. Wager, Proceedings of the Royal Society of London. Series A: Mathematical, Physical and Engineering Sciences **457**, 717 (2001), URL http://rspa.royalsocietypublishing.org/content/457/2007/717.abstract.

[17] G. Vahala, B. Keating, M. Soe, J. Yepez, L. Vahala, and S. Ziegeler, The European Physical Journal Special Topics **171**, 167 (2009), ISSN 1951-6355, URL http://dx.doi.org/10.1140/epjst/e2009-01025-7.

[18] J. Yepez, Physical Review A **74**, 042322 (2006).

[19] J. Yepez, in *Quantum Computing and Quantum Communications: 1st NASA International Conference on Quantum Computing and Quantum Communications*, edited by C. P. Williams, Lecture Notes in Computer Science (Springer-Verlag, 1999), pp. 34–60.

[20] J. Yepez, Technical Report AFRL-VS-HA-TR-2006-1143, Air Force Research Laboratory, AFRL/RV Hanscom AFB, MA 01731 (2007), DTIC ADA474659.

[21] G. Vahala, L. Vahala, and J. Yepez, Physics Letters A **310**, 187 (2003).

[22] G. Vahala, L. Vahala, and J. Yepez, Philosophical Transactions of the Royal Society **362**, 1677 (2004).

[23] J. Yepez, G. Vahala, and L. Vahala, Quantum Information Processing **4**, 457 (2005).

[24] J. Yepez, G. Vahala, L. Vahala, and M. Soe, Physical Review Letters **103**, 084501 (pages 4) (2009), URL http://link.aps.org/abstract/PRL/v103/e084501.

[25] J. Yepez, G. Vahala, L. Vahala, and M. Soe (SPIE, 2010), vol. 7702, p. 770209, URL http://link.aip.org/link/?PSI/7702/770209/1.

[26] G. Vahala, M. Soe, B. Zhang, J. Yepez, L. Vahala, J. Carter, and S. Ziegeler, Proceedings of the 2011 SC - International Conference for High Performance Computing, Networking, Storage and Analysis (2011).

[27] M. E. Peskin and D. V. Schroeder, *An Introduction to Quantum Field Theory* (Westview Press, 1995).

[28] J. Yepez, Phys. Rev. E **63**, 046702 (2001), URL http://link.aps.org/doi/10.1103/PhysRevE.63.046702.

[29] J. Yepez, USAF Technical Report, PL-TR-96-2122(I), ERP, No. 1200 (1995).

APPENDIX

The matrix representation of the eight SU(2) Gell-Mann generators that we use above are

$$\lambda_1 = \begin{pmatrix} 0 & 1 & 0 \\ 1 & 0 & 0 \\ 0 & 0 & 0 \end{pmatrix}, \quad \lambda_2 = \begin{pmatrix} 0 & -i & 0 \\ i & 0 & 0 \\ 0 & 0 & 0 \end{pmatrix}, \quad \lambda_3 = \begin{pmatrix} 1 & 0 & 0 \\ 0 & -1 & 0 \\ 0 & 0 & 0 \end{pmatrix},$$
$$\lambda_4 = \begin{pmatrix} 0 & 0 & 1 \\ 0 & 0 & 0 \\ 1 & 0 & 0 \end{pmatrix}, \quad \lambda_5 = \begin{pmatrix} 0 & 0 & -i \\ 0 & 0 & 0 \\ i & 0 & 0 \end{pmatrix},$$
$$\lambda_6 = \begin{pmatrix} 0 & 0 & 0 \\ 0 & 0 & 1 \\ 0 & 1 & 0 \end{pmatrix}, \quad \lambda_7 = \begin{pmatrix} 0 & 0 & 0 \\ 0 & 0 & -i \\ 0 & i & 0 \end{pmatrix}, \quad \lambda_8 = \frac{1}{\sqrt{3}} \begin{pmatrix} 1 & 0 & 0 \\ 0 & 1 & 0 \\ 0 & 0 & -2 \end{pmatrix}. \tag{A-1}$$